Journal of Electroanalytical Chemistry 869 (2020) 114214

Contents lists available at ScienceDirect

Journal of Electroanalytical Chemistry

journal homepage: www.elsevier.com/locate/jelechem

Electron migration optimization through nanostructural control of hierarchical Fe_3O_4 based counter electrodes for high-performance dye-sensitized solar cells

Haifeng Xu [a], Guang Zhu [a,b,*], Zhong Jin [c,**]

[a] School of Mechanical and Electrical Engineering, Suzhou University, Suzhou 234000, China
[b] Key Laboratory of Spin Electron and Nanomaterials of Anhui Higher Education Institutes, Suzhou University, Suzhou 234000, China
[c] Key Laboratory of Mesoscopic Chemistry of MOE, Jiangsu Key Laboratory of Advanced Organic Materials, School of Chemistry and Chemical Engineering, Nanjing University, Nanjing 210023, China

ARTICLE INFO

Article history:
Received 11 April 2020
Received in revised form 29 April 2020
Accepted 13 May 2020
Available online 18 May 2020

Keywords:
Electrocatalytic activity
Counter electrode
Dye-sensitized solar cells
Fe_3O_4
Structural modulation

ABSTRACT

Reasonably designing of counter electrode (CE) and iodine ion electrolyte is crucial for enhancing the power conversion efficiency (PCE) of dye-sensitized solar cells (DSSCs). Fe_3O_4 possesses high conductivity and catalytic activity to facilitate the electrolyte reduction reaction at the surface of CE. However, the morphology control and active site modulation of Fe_3O_4 based CE are still to be explored. Herein, we propose a facile bottom-top strategy to prepare hierarchical Fe_3O_4 nanostructures with different tunable morphologies, including Fe_3O_4 nanorings (NR), nanosheets (NS) and nanoflowers (NF). Electrochemical impedance spectroscopy, Tafel polarization, cyclic voltammetry and photocurrent density-voltage measurements of these samples were carried out, revealing their high performances as CE in DSSCs. Among them, the Fe_3O_4 NF with mesoporous nanosphere flower structure and high specific surface area is synthesized, which realized the highest PCE (8.56%), which is also higher than the value of Pt based CE (7.57%). Compared to other competing materials, Fe_3O_4 nanostructure based CE shows the outstanding merits of high photovoltaic performance, easy preparation, low cost and eco-friendliness, offering the possibility to replace conventional Pt based CE in DSSCs.

1. Introduction

Energy is vital to human survival and social development [1–3,]. However, the use of non-renewable energy caused serious environmental problems and excessive greenhouse gas emission [4–6]. Therefore, it is of great importance to exploit a variety of clean energy sources that can be effectively harvested for human use without large-scale power plants, such as solar, tidal and wind power [7–10]. Among them, solar energy is one of the most abundant and sustainable energy in the nature, and can be easily acquired without the need of transmission medium to meet the human demand for energy [11–15]. Solar cells are one of the preferred clean energy devices, especially, Dye-sensitized solar cells (DSSCs) are a class of solar cells with the advantages of relatively high PCE, easy preparation and low cost [16,17]. The photoanode of DSSCs responsible for the light absorption is usually composed of nano-crystalline TiO_2 layer and dye modified on transparent conductive glass; the electrolyte of DSSCs is normally I^-/I_3^- redox pairs responsible for the reduction and regeneration of dye molecules [18–20]. The counter electrode (CE) is responsible for the regeneration of redox pairs in catalytic electrolytes [21,22], and is also the focus of this study. The catalytic performance of CE can greatly influence the fluidity and efficiency of the whole cell [23]. The acknowledged CE material is precious metal platinum, but platinum is expensive and not suitable for large-scale industrial production [24]. Therefore, the development of high-performance, low-cost, resource-rich CE materials has attracted much attention. Some previous studies have reported the use of platinum based alloys with different proportions of other metals (Mo, Co, Ni, Fe, etc) as CE in DSSCs [25–27]. Although the research on electrode materials has made great progress.

However, these materials still contain a certain amount of Pt, and the high cost is a key factor that restricts the practical application. It is important to develop non-precious metal compound based CE materials with different morphologies and high specific surface areas to the catalytic activity and interfacial charge transfer properties [28,29].

In this research, we report the synthesis of Fe_3O_4 with different morphologies (Fe_3O_4 nanorings (NR), Fe_3O_4 nanosheets (NS) and Fe_3O_4

---

* Corresponding author at: School of Mechanical and Electrical Engineering, Suzhou University, Suzhou 234000, China.
** Corresponding author.
E-mail addresses: guangzhu@ahszu.edu.cn, (G. Zhu), zhongjin@nju.edu.cn. (Z. Jin).

http://dx.doi.org/10.1016/j.jelechem.2020.114214
1572-6657/

nanoflowers (NF)) by a simple hydrothermal method to serve as high-performance CE materials for DSSCs. The conductivity and surface active sites of Fe_3O_4 nanostructures are optimized by morphological control to improve electron migration and catalytic activity, thus brining good electrochemical performance and high PCE. The *J-V* curve measurements reveal that the PCE of DSSCs with Fe_3O_4 NF as CE material has been greatly improved (8.56%), which is superior to the performance of DSSCs with Fe_3O_4 NR or Fe_3O_4 NS as CE materials, and also higher than of DSSCs with Pt CE (7.84%). It indicates that Fe_3O_4 NF could serve as a potential candidate to replace conventional Pt CE in DSSCs and also could be utilized to adjust electron transfer in many other electrochemical applications.

2. Experimental

All chemicals used in this study were analytical grade and used without further purification.

Ferric chloride hexahydrate ($FeCl_3$•$6H_2O$), ethylene glycol, polyethylene glycol (PEG), ethylenediamine (EDA), urea, sodium salicylate were all purchased from Aladdin Industrial Corporation. Deionized water was obtained from electrothermal distiller and was used in all experiments.

2.1. Preparation of Fe_3O_4 NR and Fe_3O_4 NS

The precursor of Fe_3O_4 NR and Fe_3O_4 NS was synthesized by a one-step solvothermal approach, as displayed in Schematic 1 a. Firstly, $FeCl_3 \cdot 6H_2O$ (5 mmol) and polyethylene glycol (PEG) 2000 (0.5 g) were poured in ethylene glycol (40 mL) and stirred evenly. Then, 10 mmol of ethylenediamine (EDA) were added into the homogeneous mixed solution. After 2 h of vigorous stirring, the mixed solution was transferred into a 100 mL Teflon-lined stainless steel autoclave and heated at 180 °C for 8 h. The yellow precursor was collected and washed several times with water and absolute ethanol, and finally dried in a vacuum oven at 50 °C for 12 h. The as-prepared precursor was heated at 350 °C for 2 h under nitrogen atmosphere to form Fe_3O_4 NS. Alternatively, the yellow precursor was calcined at 450 °C for 2 h under nitrogen atmosphere to form Fe_3O_4 NR.

2.2. Preparation of Fe_3O_4 NF

Fe_3O_4 NF was formed through a simple hydrothermal method. The synthesis process is demonstrated in Schematic 1 b. Briefly, ferric chloride hexahydrate ($FeCl_3 \cdot 6H_2O$, 1.6 g) and urea (0.6 g) were slowly poured into 70 mL of ethylene glycol and stirred by magnetic bar. Then, 1.0 g of sodium salicylate ($C_7H_5NaO_3$) was put into the solution, and continuously stirred for 1 h. Later, the mixture was transferred to a Teflon-lined stainless-steel autoclave. The autoclave was sealed and maintained at 180 °C for 8 h. The product was centrifugated and washed with water for four times, and dried in a vacuum oven at 50 °C for 12 h. The powder was then heated at 500 °C for 2 h in N_2 atmosphere to form Fe_3O_4 NF.

2.3. Fabrication of counter electrodes

At the beginning, the fluorine-doped tin oxide (FTO) transparent glass substrates (NSG, $13\Omega sq^{-1}$) were ultrasonically cleaned sequentially in absolute ethyl alcohol and then stored in isopropyl alcohol. The given materials powders (0.04 g) were used as raw material to prepare CEs. The given powders composite was ground with poly ethylene glycol powder (0.01 g) and 1 mL of absolute ethanol with a mortar to form a gelatin microspheres powders. CE coats were prepared by a doctor-blade method on the FTO glass substrates with subsequent natural drying and annealing at 400 °C for 60 min under a flowing of nitrogen gas environment. After natural cooling to room temperature, CE was obtained.

2.4. Assembly of DSSCs

A sandwich DSSC device is combined of a dye-sensitized photoanode TiO_2, the as-prepared CEs, and liquid electrolyte. The commercial photoanodes with an actual area of 0.5*´0.5 cm^2 TiO_2 film (Dalian HeptaChroma Solar Tech Co, Ltd) were dipped in N719 (Dalian HeptaChroma Solar Tech Co, Ltd) dye solution overnight at room temperature, then cleaned with ethanol and dried in the air. The liquid electrolyte was composed of 0.1 M LiI, 0.12 M I2, 1.0 M 1, 2-dimethyl-3-propylimidazolium iodide and 0.5 M 4-tert-buylpyridine in acetonitrile

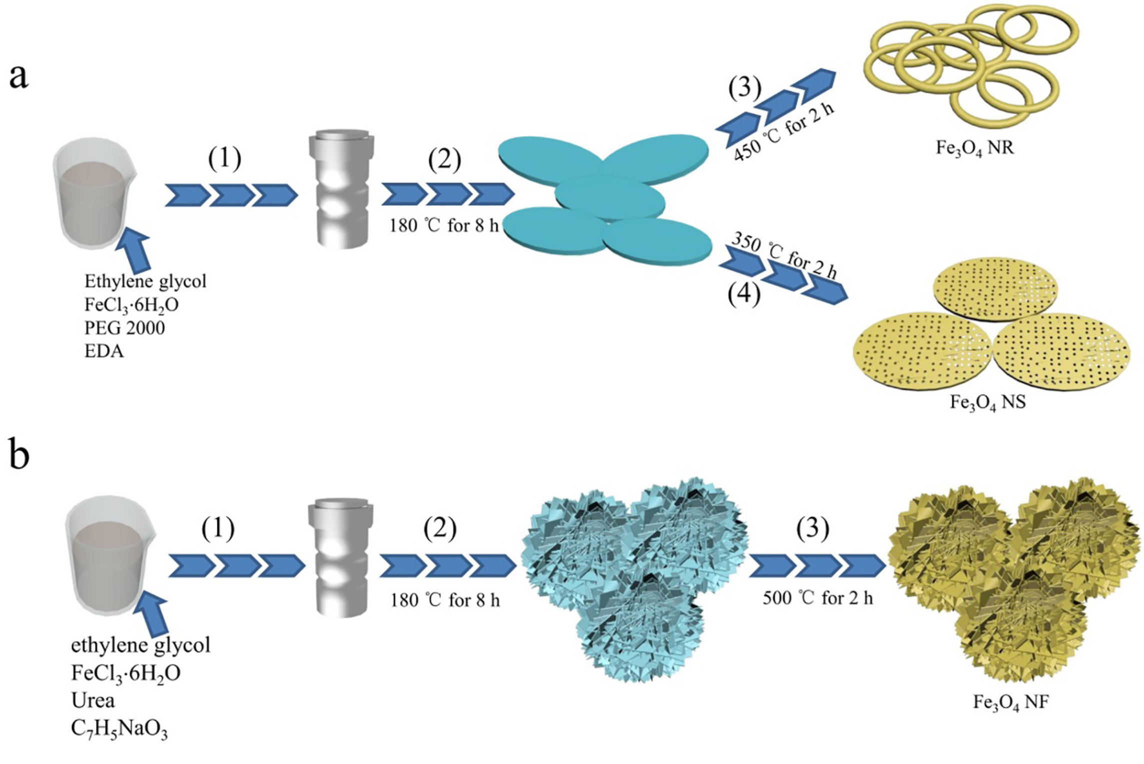

Schematic 1. (a) Synthetic routes of Fe_3O_4 NR and Fe_3O_4 NS. (b) Synthetic route of Fe_3O_4 NF.

solution. The two electrodes were clipped together with solid paraffin working as the sealant to prevent the electrolyte solution from leaking. The actual area of CEs made is 0.5*´0.5 cm^2. Due to the actual area of TiO_2 anode, the effective area for each cell is 0.5*0.5 cm^2. For comparative purpose, the production process for each cell is the same.

2.5. Characterization and electrochemical measurements

Photocurrent density-voltage (J-V) curves were implemented by a solar light simulator under an illumination of 100 mW cm^{-2}, AM 1.5 and using a digital source meter (Keithley 2410). Cyclic voltammetry (CV) curves were tested in the range from -0.4 to 1.1 V at a scan rate of 25 mV/s in a supporting electrolyte consisting of 10 mM LiI, 1 mM I_2, and 100 mM $LiClO_4$ in acetonitrile and carried out in a three-electrode system. Pt thin film was used as the CE, Ag/AgCl with saturated KCl solution as the reference electrode and as-prepared materials as the working electrode. In DSSCs, a symmetrical cell is widely used in EIS and Tafel polarization measurements. Electrochemical impedance spectroscopy (EIS) of symmetrical cells was verified in a frequency range of $0.1 \sim 10^6$ Hz and at alternating current voltage amplitude of 10 mV. Tafel polarization measurements were also achieved in a symmetrical cell and kept quasi stationary conditions with the voltage range $-$ 1 to 1 V at a scan rate of 50 mV/s. EIS and Tafel measurements were carried out in dark environment.

The surface morphologies of CEs were observed via a field-emission scanning electron microscope (JSM-6701F, JEOL accelerating voltage of 5 kV), transmission electron microscopy (TEM, JEOL-2010, operating voltage of 200 kV). All samples were prepared by depositing a drop of diluted suspensions in ethanol on a carbon-film-coated copper grid. The crystalline structures of Fe_3O_4 and Fe_3O_4@3DRGO powders were recorded via a Rigaku/Max-3A X-ray diffractometer with Cu Kα radiation (λ = 1.54178 Å). X-ray photoelectron spectroscopy was conducted using a Smart Lab 9KW to study the chemical states.

3. Results and discussion

3.1. Composition and morphology analyses

The structural features of Fe_3O_4 nanostructures were identified by SEM and TEM images, as shown in Fig. 1. The SEM images in Fig. 1a and b disclose that Fe_3O_4 NR, Fe_3O_4 NS and Fe_3O_4 NF have different morphological characteristics. we can clearly observe that the surface of Fe_3O_4 NF possesses abundant porosity. Moreover, the morphological characteristics of different Fe_3O_4 nanostructures were observed by TEM to analyze their corresponding internal structures. Fig. 1d shows that Fe_3O_4 NR possess delicate ring-shape structure. A large number of pores are clearly found on Fe_3O_4 NR, as shown in the Fig. 1e. Furthermore, the hierarchical structure of Fe_3O_4 NF was made up by a lots of thin sheets and porous structures, as clearly presented in Fig. 1c and f. The high-resolution TEM (HRTEM) image of Fe_3O_4 NF is displayed in Fig. 1g, which also exhibits the good crystalline structure of Fe_3O_4 NF. The XPS spectrum of Fe_3O_4 NF at Fe 2p region is showed in Fig. 1h. The Fe 2p3/2 peak can be deconvoluted into two obvious peaks corresponding to Fe^{2+} (711.15 eV) and Fe^{3+} (712.65 eV), respectively. This result indicates the mixed valence state of Fe species and suggests the formation of Fe_3O_4 phase. The XRD patterns of the as-prepared Fe_3O_4 NR, Fe_3O_4 NS and Fe_3O_4 NF were also studied, as shown in Fig. 1i. The typical Fe_3O_4 diffraction peaks located in 18.4°, 30.2°, 35.5°, 37.1°, 43.2°, 53.1°, 57.1°, 62.8°, and 87.1° can be well assigned to (111),

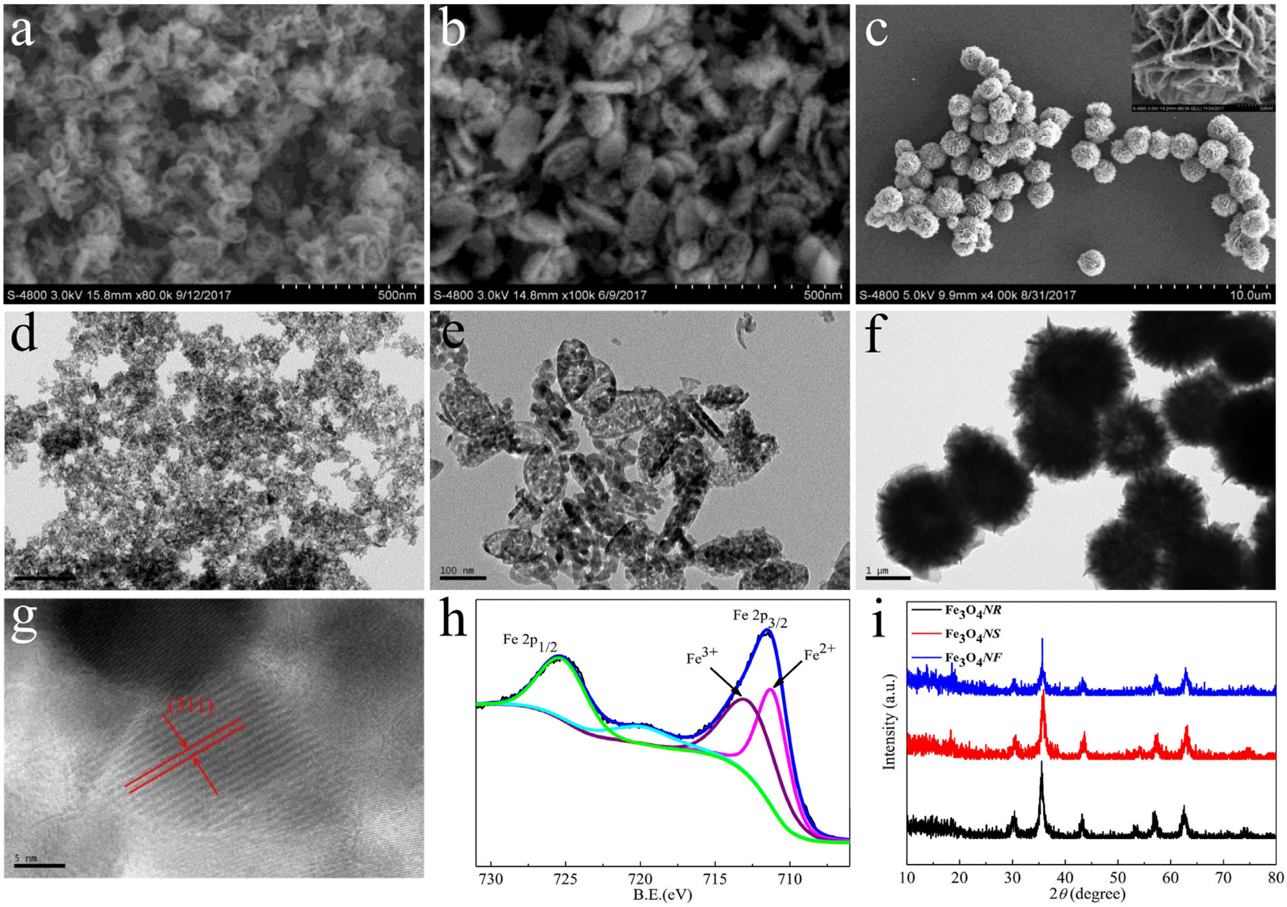

Fig. 1. (a-c) SEM images of Fe_3O_4 NR, Fe_3O_4 NS and Fe_3O_4 NF, respectively. (d-g) TEM images of Fe_3O_4 NR, Fe_3O_4 NS and Fe_3O_4 NF, respectively. (h) XPS spectrum of Fe_3O_4 NF. (i) XRD patterns of Fe_3O_4 NR, Fe_3O_4 NS and Fe_3O_4 NF.

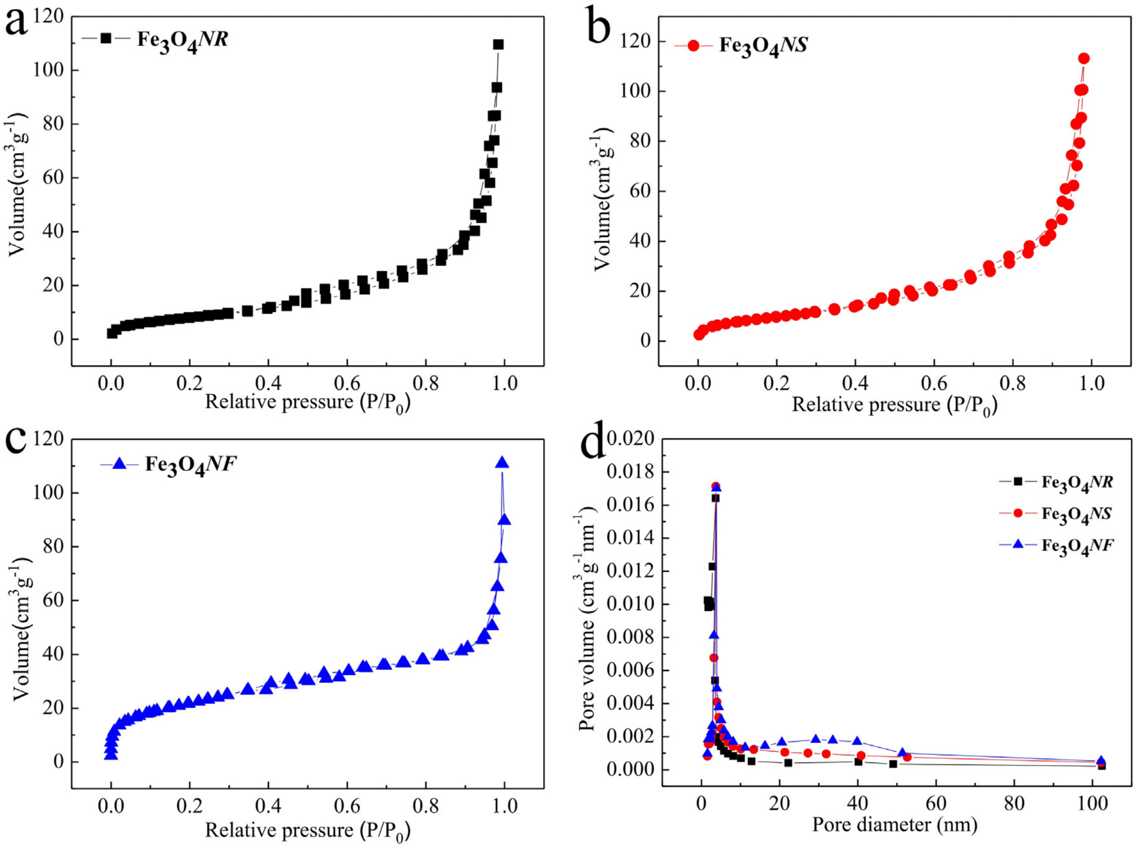

Fig. 2. (a-c) N_2 adsorption-desorption isotherms of Fe_3O_4 NR, Fe_3O_4 NS and Fe_3O_4 NF. (d) The pore size distribution of Fe_3O_4 NR, Fe_3O_4 NS and Fe_3O_4 NF.

(220), (311), (222), (440), (422), (511) (440) and (642) crystal planes of Fe_3O_4, which can be well indexed to JCPDS: 75–0033. It can be concluded that Fe_3O_4 NR, Fe_3O_4 NS and Fe_3O_4 NF have been successfully achieved.

The porous structure can correspondingly increase the specific surface area and shorten the electron transport path to speed up the electron transport, thus can help to improve the catalytic performance. Brunauer-

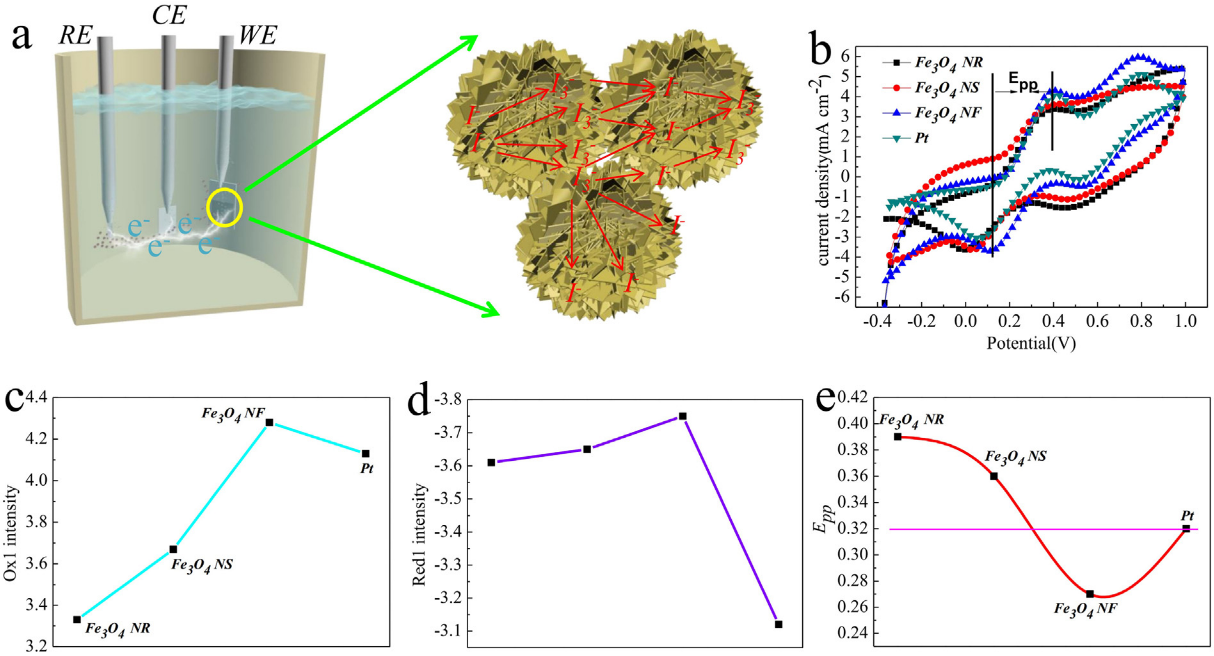

Fig. 3. (a) Schematic diagram of the three-electrode cell and the I_2 adsorption, dissociation, and desorption process of Fe_3O_4 NF during CV measurement. (b) CV curves of Fe_3O_4 NR, Fe_3O_4 NS, Fe_3O_4 NF and Pt electrodes for the redox of I^-/I_3^- species. (c) Ox1 intensity of all-prepared samples during CV measurement. (d) Red1 intensity of all-prepared samples during CV measurement. (e) E_{pp} of all-prepared samples during CV measurement.

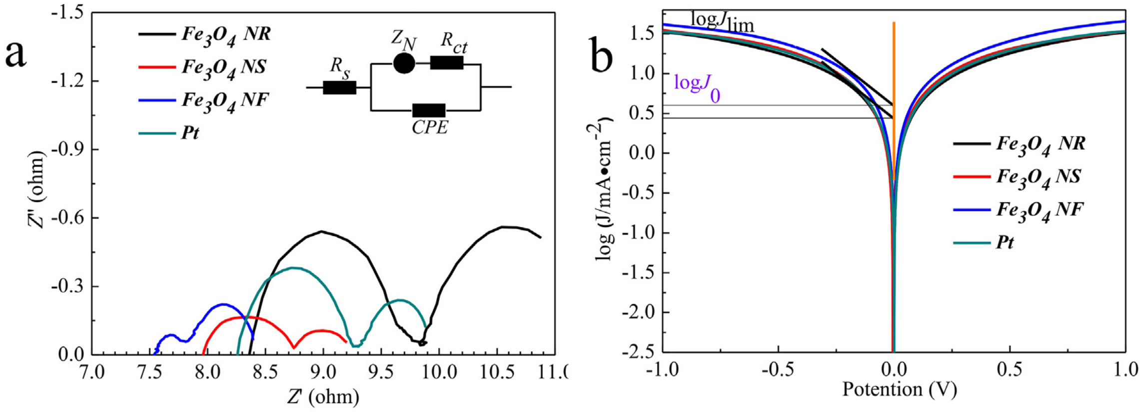

Fig. 4. (a) Nyquist plots of DSSCs using Fe_3O_4 NR, Fe_3O_4 NS, Fe_3O_4 NF and Pt thin film as the CE. (b) Tafel polarization curves of the Fe_3O_4 NR, Fe_3O_4 NS, Fe_3O_4 NF and Pt thin film.

Emmett-Teller (BET) tests reveal that the Fe_3O_4 NF have a specific surface area of 128 $m^2 \cdot g^{-1}$, which is higher than Fe_3O_4 NR (86 $m^2 \cdot g^{-1}$) and Fe_3O_4 NS (93 $m^2 \cdot g^{-1}$), as presented in Fig. 2a-c. Meanwhile, the pore size distributions of Fe_3O_4 NR, Fe_3O_4 NS and Fe_3O_4 NF were evaluated using the BJH method, as shown in Fig. 2d. The average pore sizes of these samples are about 15.98 nm, 6.45 nm and 8.56 nm, respectively. The high specific surface area can increase the contact area between electrode and electrolyte interface, provide more active sites and accelerate diffusion kinetics, which would be helpful to enhance the electrochemical and photoelectric conversion performances.

3.2. Electrochemical analyses

Cyclic voltammetry (CV) tests were used to test the catalytic activity of as-prepared CE materials. The electrochemical cell configuration with a three-electrode system is presented in Fig. 3a, and the electrolyte is I_3^-/I^- couple [27–29]. The role of the CE material in the electrolyte cycling reaction is to provide electrons for reducing the oxidized electrolyte and regenerating dyes effectively [30]. The typical CV redox peaks are shown in the Fig. 3b. There are two pairs of redox peaks respectively, and the redox peaks value near the low potential changes are corresponding to Ox1 and Red1, and also have a greater impact on the photovoltaic performance [31,32]. The high peak current densities of the cathode peaks indicate that the electrode has high electrocatalytic activity. The variation trends of Ox1 and Red1 are clearly presented in Fig. 3c-d, and can be expressed by the following Eqs. (1) and (2):

$$I_3^- + 2e^- = 3I^- \tag{1}$$

$$3I_2 + 2e^- = 2I_3^- \tag{2}$$

The redox peaks in the high frequency region correspond to Ox2 and Red2. The distance between Ox1 and Red1 is represented as E_{pp}. The smaller value of E_{pp} indicates the higher reduction efficiency of iodine ions [33]. From Fig. 3e, it can be concluded that the Fe_3O_4 NF exhibit the smallest value of E_{pp} (0.286 V), indicating that the Fe_3O_4 NF has good electrochemical properties as CE material. On the whole, the CV shape of Fe_3O_4 NF is close to that of Pt, suggesting the remarkable catalytic activity.

Electrochemical impedance spectroscopy (EIS) and Tafel tests were performed by preparing typical sandwich-structure cells (CE/electrolyte/CE), which further consider the charge transfer process between the electrolyte and the CE interface [34,35]. The Nyquist plots with the corresponding equivalent circuits are described in Fig. 4a, and a proper equivalent circuit model is also shown in the insert. It is very interesting that there are two semicircles in these EIS spectra. The first half circle is located in the high frequency region and can be ascribed to the charge transfer resistance (R_{ct}) [36]. Its range can reflect the capability of redox process at the electrolyte/CE interface [37]. The other half circle in low frequency region is corresponding to the Nernst diffusion impedance (Z_N) of the redox couple transport in the electrolyte [38,39]. In addition, the high-frequency intercept on the real axis reflects the series resistance (R_s) in the Nyquist plot [40]. The corresponding values for EIS parameters of R_s and R_{ct} are summarized in Table 1. We found that the R_{ct} value of different CE materials increased in the order of Fe_3O_4 NF < Fe_3O_4 NS < Fe_3O_4 NR < Pt. The Fe_3O_4 NF exhibited the lowest R_{ct}, which can reflect that the catalytic activity of Fe_3O_4 NF is remarkably higher than the other CE materials. The possible reason for the significantly reduced impedance of the Fe_3O_4 NF could be attributed to the improved interfacial contact and electrical migration between the transparent conducting film and the CE resulted from the large specific surface area of Fe_3O_4 NF.

Tafel polarization were measured to further evaluate the catalytic activity of as-prepared CEs, as displayed in Fig. 4b. The Tafel curves possess three regions: the polarization area, the Tafel area and the diffusion area [41]. The catalytic activity of all CEs for I_3^- reduction can be accessed via the Tafel and diffusion areas, from which the corresponding exchange current density (J_0) and the limiting diffusion current density (J_{lim}) can be attained [42,43]. The J_0 can be attained by the deduction of the Tafel curves [44]. The Fe_3O_4 NF displays greater slopes than those of Fe_3O_4 NS, Fe_3O_4 NR and Pt electrode, indicating the outstanding catalytic activity of Fe_3O_4 NF CE in the electrolyte of DSSCs.

Table 1
Parameters derived from EIS and Tafel curves recorded under the same conditions for DSSCs equipped with Fe_3O_4 NR, Fe_3O_4 NS and Fe_3O_4 NF CEs, respectively.

CEs	R_s ($\Omega \cdot cm^2$)	R_{ct} ($\Omega \cdot cm^2$)	lgJ_0 ($mA \cdot cm^{-2}$)	lgJ_{lim} ($mA \cdot cm^{-2}$)	E_{PP} (V)
Fe_3O_4 NR	8.3	0.78	0.45	1.49	0.39 ± 0.01
Fe_3O_4 NS	7.9	0.43	0.48	1.55	0.36 ± 0.01
Fe_3O_4 NF	7.5	0.14	0.61	1.63	0.27 ± 0.01
Pt	8.2	0.16	0.57	1.52	0.32 ± 0.01

3.3. DSSC tests

A schematic diagram of the working principle of the whole DSSC is presented in Fig. 5a. The DSSCs based on Fe_3O_4 CEs with different morphologies are tested under simulated sun light (AM 1.5 G illumination), and the density-voltage curves (*J-V* curves) were assessed [45–47], as shown in Fig. 5b. The equivalent parameters of *J-V* curves, including short-circuit current density (J_{sc}), open-circuit voltage (V_{oc}), fill factor (FF), and power conversion efficiency (PCE) are listed in Table 2. Besides, the PCE values of these Fe_3O_4 CE-based DSSCs are proportional to their J_{sc} values. It is obvious that the Fe_3O_4 NF CE based DSSCs show superior performances compared to those based on Fe_3O_4 NS and Fe_3O_4 NR CEs, attributing to the improvement of specific surface area as a result of optimized morphology modulation [48,49]. The DSSCs based on Fe_3O_4 NF CEs achieve a high PCE value of 8.56%, which is greater than those based on Fe_3O_4 NS, Fe_3O_4 NR and Pt CEs, demonstrating the remarkable catalytic activity for I^- regeneration. These results indicate that the morphology and structure modulation can greatly enhance the specific surface area to further promote charge transfer and provide more electro-catalytic active cites [50].

To further assess the photoelectric conversion performances, the IPCE curves of the DSSCs with as-prepared CEs were also tested, as shown in Fig. 5c. It is notable that the DSSCs based on Fe_3O_4 NF CEs possess the highest photo-response (74%) at the wavelength of ~525 nm, which exceed the DSSCs based on Fe_3O_4 NR, Fe_3O_4 NS and Pt electrodes. These consequences are in good agreement with the above analyses of EIS, CV, and Tafel curves, and verify the good PCE performances of Fe_3O_4 NR based CEs. The significantly improved performances should be ascribed to the higher electrical conductivity and catalytic performance of Fe_3O_4 NR than those of Fe_3O_4 NR and Fe_3O_4NS. It indicates that the large surface-to-volume ratio can efficiently expose more catalytic sites and accelerate the reversible redox reaction of iodine ions and inhibiting ion coupling, thus greatly enhanced the photoelectric conversion performances of DSSCs.

Table 2
Photovoltaic parameters for DSSCs recorded under the same conditions for DSSCs equipped with Fe_3O_4 NR, Fe_3O_4 NS and Fe_3O_4 NF CEs, respectively.

CEs	J_{SC} (mA·cm^{-2})	V_{OC} (V)	*FF* (%)	*PCE* (%)
Fe_3O_4 NR	15.5	0.750	62.63	7.28
Fe_3O_4 NS	16.3	0.765	61.59	7.68
Fe_3O_4 NF	16.5	0.755	68.72	8.56
Pt	16.2	0.755	61.88	7. 57

4. Conclusions

In summary, we have established a feasible strategy to modulate the morphology of Fe_3O_4 based CEs for optimizing the multi-dimensional electron transfer behavior in electrolyte, leading to the greatly improved performances of DSSCs. This study implies that the essential roles of hierarchical structure with larger specific surface area can greatly affect the electron migration and interfacial charge transfer, offering a new approach for the rational design of novel CE materials in DSSCs.

Declaration of Competing Interest

The authors declared that they have no conflicts of interest to this work. We declare that we do not have any commercial or associative interest that represents a conflict of interest in connection with the work submitted.

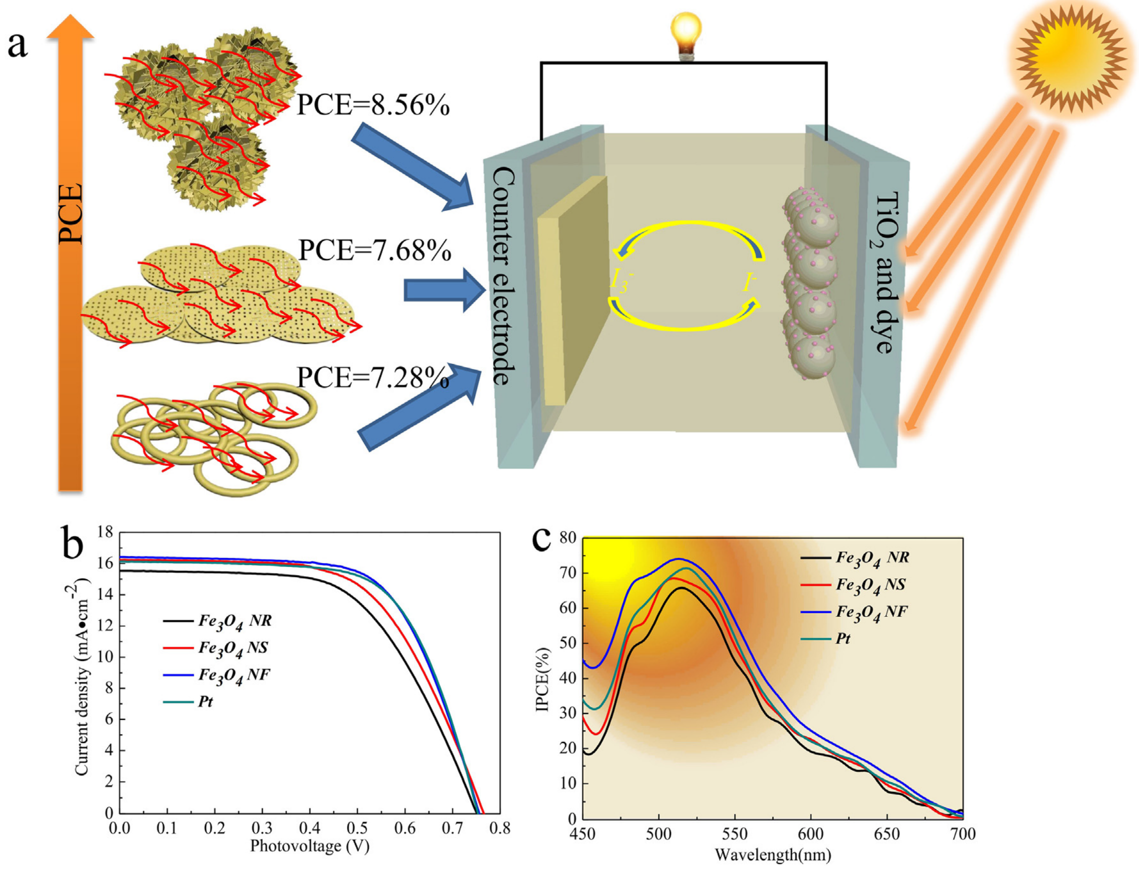

Fig. 5. (a) Schematic structure of a DSSC assemble with as-prepared Fe_3O_4 CE. (b) *J-V* curves of DSSCs assembled with different CEs. (c) IPCE curves of DSSCs assembled with different CEs.

Acknowledgements

This work is supported financially by the Provincial Natural Science Foundation of Anhui (1908085ME120), the Outstanding Youth Talents in Anhui Provincial Education Department (2019gxbjZD43), the Academic Technical Leader of Suzhou University (No.2018xjxs03), the Innovative Research Team of Anhui Provincial Education Department (No.2016SCXPTTD), the Key Discipline of Material Science and Engineering of Suzhou University (No.2017XJZDXK3). This work is also supported by the National Key R&D Program of China (2017YFA0208200), the Projects of NSFC (21872069, 51761135104), the Natural Science Foundation of Jiangsu Province (BK20180008), and the Fundamental Research Funds for the Central Universities of China (0205-14380188).

References

[1] C.-C.P. Chiang, C.-Y. Hung, S.-W. Chou, J.-J. Shyue, K.-Y. Cheng, P.-J. Chang, Y.-Y. Yang, C.-Y. Lin, T.-K. Chang, Y. Chi, H.-L. Chou, P.-T. Chou, Adv. Funct. Mater. 28 (2018) 1703282.

[2] F. Du, X. Zuo, Q. Yang, G. Li, Z. Ding, M. Wu, Y. Ma, K. Zhu, J. Mater. Chem. C 4 (2016) 10323–10328.

[3] J. Briscoe, S. Dunn, Adv. Mater. 28 (2016) 3802–3813.

[4] J.X. Yao, K. Zhang, W. Wang, X.Q. Zuo, Q. Yang, H.B. Tang, M.Z. Wu, G. Li, Nanoscale 10 (2018) 7946–7956.

[5] M.D. Ye, X.R. Wen, M.Y. Wang, J. Iocozzia, N. Zhang, C.J. Lin, Z.Q. Lin, Mater. Today 18 (2015) 155–162.

[6] X.H. Liu, K. Yan, D.W. Tan, X. Liang, H.M. Zhang, W. Huang, ACS Energy Lett. 3 (2018) 2701–2707.

[7] Y.X. Lin, L. Yang, Y.K. Zhang, H.L. Jiang, Z.J. Xiao, C.Q. Wu, G.B. Zhang, J. Jiang, L. Song, Adv. Energy Mater. 8 (2018) 1703623.

[8] C.X. Hou, Z.X. Tai, L.L. Zhao, Y.J. Zhai, Y. Hou, Y.Q. Fan, F. Dang, J. Wang, H.K. Liu, J. Mater. Chem. A 6 (2018) 9723–9736.

[9] H.W. Huang, R.R. Cao, S.X. Yu, K. Xu, W.C. Hao, Y.G. Wang, F. Dong, T.R. Zhang, Y.H. Zhang, Appl. Catal. B Environ. 219 (2017) 526–537.

[10] H. Wang, K. Sun, F. Tao, D.J. Stacchiola, Y.H. Hu, Angew. Chem. Int. Ed. 52 (2013) 9210–9214.

[11] F. Gong, H. Wang, X. Xu, G. Zhou, Z.S. Wang, J. Am. Chem. Soc. 134 (2012) 10953–10958.

[12] L. Chen, W.L. Chen, X.L. Wang, Y.G. Li, Z.M. Su, E.B. Wang, Chem. Soc. Rev. 48 (2019) 260–284.

[13] P.J. Chang, K.Y. Cheng, S.W. Chou, J.J. Shyue, Y. Yun, C.Y. Hung, C.Y. Lin, H.L. Chen, H.L. Chou, P.T. Chou, Chem. Mater. 28 (2016) 2110–2119.

[14] E. Bi, H. Chen, X. Yang, W.Q. Peng, M. Grätzel, L.Y. Han, Energy Environ. Sci. 7 (2014) 2637–2641.

[15] Q. Luo, H. Ma, Q. Hou, Y.X. Li, J. Ren, X.Z. Dai, Z.B. Yao, Y. Zhou, L.C. Xiang, H.Y. Du, H.C. He, N. Wang, K.L. Jiang, H. Lin, H.W. Zhang, Z.H. Guo, et al., Adv. Funct. Mater. 28 (2018) 1706777.

[16] D.H. Kweon, J.B. Baek, Adv. Mater. 31 (2018) 1804440.

[17] X. Meng, C. Yu, X. Song, J. Iocozzia, J. Hong, M. Rager, H. Jin, S. Wang, L. Huang, J. Qiu, Z. Lin, Angew. Chem. Int. Ed. 57 (2018) 4682–4686.

[18] J.M. Rhodes, C.A. Jones, L.B. Thal, J.E. Macdonald, Chem. Mater. 29 (2017) 8521–8530.

[19] P. Kulkarni, S.K. Nataraj, R.G. Balakrishna, D.H. Nagaraju, M.V. Reddy, J. Mater. Chem. A 5 (2017) 220,40–22094.

[20] J. Yao, K. Zhang, W. Wang, X.Q. Zuo, Q. Yang, H.B. Tang, M.Z. Wu, G. Li, ACS Appl. Mater. Interfaces 10 (2018) 19564–19572.

[21] X. Meng, C. Yu, X. Zhang, L. Huang, M. Rager, J. Hong, J. Qiu, Z. Lin, Nano Energy 54 (2018) 138–147.

[22] A. Sarkar, A.K. Chakraborty, S. Bera, Sol. Energy Mater. Sol. Cells 182 (2018) 314–320.

[23] H. Zhang, Y. Wang, P. Liu, S.L. Chou, J.Z. Wang, H.W. Liu, G.Z. Wang, H.J. Zhao, ACS Nano 10 (2016) 507–514.

[24] B. Sun, X. Feng, Y. Yao, Q. Su, W.J. Ji, C.T. Au, ACS Catal. 3 (2013) 3099–3105.

[25] S.N. Yun, Y.F. Liu, T.H. Zhang, S. Ahmad, Nanoscale 7 (2015) 11877–11893.

[26] S.N. Yun, A. Hagfeldt, T.L. Ma, Adv. Mater. 26 (2014) 6210–6237.

[27] T. Liu, C. Jiang, B. Cheng, W. You, J.G. Yu, J. Mater. Chem. A 5 (2017) 21257–21265.

[28] X. Meng, C. Yu, X. Song, Y. Liu, S.X. Liang, Z.Q. Liu, C. Hao, J.S. Qiu, Adv. Energy Mater. 5 (2015) 1500180.

[29] F. Du, X. Zuo, Q. Yang, G. Li, Z.L. Ding, M.Z. Wu, Y.Q. Ma, K.R. Zhu, J. Mater. Chem. C 4 (2016) 10323–10328.

[30] J. Yao, K. Zhang, W. Wang, X.Q. Zuo, Q. Yang, M.Z. Wu, G. Li, Electrochim. Acta 279 (2018) 168–176.

[31] D. Guo, X. Chen, H. Wei, M.L. Liu, F. Ding, Z. Yang, K.Q. Yang, S. Wang, X.J. Xu, S.M. Huang, J. Mater. Chem. A 5 (2017) 6245–6256.

[32] M. Guo, B. Tang, H. Zhang, S.H. Yin, W. Jiang, Y.M. Zhang, M.Y. Li, H. Wang, L.Q. Jiao, Chem. Commun. 50 (2014) 7356–7358.

[33] S.K. Swami, N. Chaturvedi, A. Kumar, R. Kapoor, V. Dutta, J. Frey, T. Moehl, M. Grätzel, S. Mathew, M.K. Nazeeruddin, J. Power Sources 275 (2015) 80–89.

[34] F. Liu, J. Zhu, L. Hu, B. Zhang, J.X. Yao, M.K. Nazeeruddin, M. Grätzel, S.Y. Dai, J. Mater. Chem. A 3 (2015) 6315–6323.

[35] D.H. Kweon, J.B. Baek, Adv. Mater. 31 (2019) 1804440.

[36] X. Meng, C. Yu, X. Song, J. Iocozzia, J.F. Hong, M. Rager, H.L. Jin, S. Wang, L.L. Huang, J.S. Qiu, Z.Q. Lin, Angew. Chem. Int. Ed. 57 (2018) 4682–4686.

[37] B. Yang, X. Zuo, P. Chen, L. Zhou, X. Yang, H.J. Zhang, G. Li, M.Z. Wu, Y.Q. Ma, S.W. Jin, X.S. Chen, ACS Appl. Mater. Interfaces 7 (2015) 137–143.

[38] C. Yu, X. Meng, X. Song, S. Liang, Q. Dong, G. Wang, C. Hao, X.C. Yang, T.L. Ma, P.M. Ajayan, J.S. Qiu, Carbon 100 (2016) 474–483.

[39] O. Langmar, E. Fazio, P. Schol, G.D.L. Torre, R.D. Costa, T. Torres, D.M. Guldi, Angew. Chem. Int. Ed. 58 (2019) 4056–4060.

[40] W. Wang, J. Yao, X. Zuo, Y. Qun, M.Z. Wu, H.B. Tan, S.W. Jin, G. Li, Nanoscale Horizons 4 (2019) 1211–1220.

[41] S.W. Yoon, V.D. Dao, L.L. Larina, et al., Optimum strategy for designing PtCo alloy/reduced graphene oxide nanohybrid counter electrode for dye-sensitized solar cells, Carbon 96 (2016) 229–236.

[42] Y. Ma, J. Huang, L. Lin, J.K. Lee, H.S. Choi, J. Power Sources 365 (2017) 98–108.

[43] P. Zhai, C.C. Lee, Y.H. Chang, C. Liu, T.C.W.S.P. Feng, ACS Appl. Mater. Interfaces 7 (2015) 2116–2123.

[44] H. Jiang, Y. Lin, B. Chen, Y.K. Zhang, H.J. Liu, X.Z. Duan, D. Chen, L. Song, Mater. Today 21 (2018) 602–610.

[45] X. Meng, C. Yu, X. Song, Z.Q. Liu, B. Lu, C. Hao, J.S. Qiu, J. Mater. Chem. A 5 (2017) 2280–2287.

[46] M.X. Guo, B.B. Tang, H.M. Zhang, S.H. Yin, W. Jiang, Y.M. Zhang, M.Y. Li, H. Wang, L.Q. Jiao, Chem. Commun. 50 (2014) 7356–7358.

[47] X.T. Meng, C. Yua, X.P. Zhang, L.L. Huang, M. Ragerc, J.F. Hong, J.S. Qiu, Z.Q. Lin, Nano Energy 54 (2018) 138–147.

[48] J.X. Yao, W. Wang, X.Q. Zuo, Q. Yang, M.W. Khan, M.Z. Wu, H.B. Tang, S.W. Jin, G. Li, Appl. Catal. B Environ. 256 (2019) 117857.

[49] C.B. Cooper, E.J. Beard, Á.V. Mayagoitia, L. Stan, B.G. Gavin, D. Stenning, W. Nye, J.A. Vigil, T. Tomar, J.W. Jia, G.B. Bodedla, S. Chen, L. Gallego, S. Franco, A. Carella, K.R.J. Thomas, S. Xue, X.J. Zhu, J.M. Cole, Adv. Energy Mater. 9 (2019) 1970014.

[50] L. Zhang, X.C. Yang, W.H. Wang, G.G. Gurzadyan, J.J. Li, X.X. Li, J.C. An, Ze Yu, H.X. Wang, B. Cai, A. Hagfeldt, L.C. Sun, ACS Energy Lett. 4 (2019) 943–951.